The Study of Momentum, Mass, and Heat Transfer in a þÿ D r o p l e t L a d e n T u r b u l e n t A i r f l o w O v e r a W a v e d W by Direct Numerical Simulation

Druzhinin, Oleg A.

2018-11

Druzhinin , O A , Troitskaya , Y I & Zilitinkevich , S S 2018 , ' The Study of Momentum, þÿ M a s s , a n d H e a t T r a n s f e r i n a D r o p l e t L a d e n T u r b u l e n t A i r f l o w O v e r a W by Direct Numerical Simulation ' , Journal of Geophysical Research : Oceans , vol. 123 , no. þÿ 1 1 , p p . 8 3 4 6 8 3 6 5 . h t t p s : / / d o i . o r g / 1 0 . 1 0 2 9 / 2 0 1 8 J C 0 1 4 3 4 6

http://hdl.handle.net/10138/301400
https://doi.org/10.1029/2018JC014346

unspecified
publishedVersion

Journal of Geophysical Research: Oceans

RESEARCH ARTICLE
10.1029/2018JC014346

The Study of Momentum, Mass, and Heat Transfer in a Droplet-Laden Turbulent Airflow Over a Waved Water Surface by Direct Numerical Simulation

O. A. Druzhinin[1,2], Yu. I. Troitskaya[1,2], and S. S. Zilitinkevich[2,3,4]

[1]Russian Academy of Sciences, Institute of Applied Physics, Nizhny Novgorod, Russia, [2]Radiophysics Department, University of Nizhny Novgorod, Nizhny Novgorod, Russia, [3]Finnish Meteorological Institute, Helsinki, Finland, [4]Institute of Atmospheric and Earth System Research, University of Helsinki, Finland

Key Points:
- This paper investigates exchange processes in a droplet-laden air flow over a waved water surface by performing numerical simulation
- The impact of drops on the flow including both momentum and latent and sensible heat exchange between drops and air is taken into account
- DNS results show that drops reduce mean air velocity and temperature and increase relative humidity as compared to the droplet-free flow

Correspondence to:
O. A. Druzhinin,
droujmail@mail.ru

Citation:
Druzhinin, O. A., Troitskaya, Y. I., & Zilitinkevich, S. S. (2018). The study of momentum, mass and heat transfer in a droplet-laden turbulent airflow over a waved water surface by direct numerical simulation. *Journal of Geophysical Research: Oceans*, *123*, 8346–8365. https://doi.org/10.1029/2018JC014346

Received 6 JUL 2018
Accepted 30 OCT 2018
Accepted article online 6 NOV 2018
Published online 19 NOV 2018

Abstract This paper investigates turbulent exchange processes in a droplet-laden air flow over a waved water surface by performing direct numerical simulation (DNS). Turbulent Couette flow is considered in DNS as a model of a constant-flux layer in the marine atmospheric surface layer. Two-dimensional stationary waves at the water surface are prescribed and assumed to be unaffected by the airflow and/or droplets. Evaporating droplets of different sizes are injected into the air in the vicinity of wave crests with initial velocities and temperatures of water, and thus mimicking spume sea-spray droplets. Evolution equations of the airflow velocity, temperature, and humidity are solved in a Eulerian framework simultaneously with the equations of individual droplets coordinates and velocities, temperatures, and masses tracked in a Lagrangian framework. The momentum (Q_m) and sensible (Q_S) and latent (Q_L) heat fluxes from the droplets to air are evaluated both as phase-averaged Eulerian fields and as fluxes integrated over time along Lagrangian droplets trajectories. The results show that droplets extract momentum from the surrounding air ($Q_m < 0$), and $Q_L > 0$ and increases with droplet diameter, d, whereas $Q_S < 0$, reaches maximum for droplets with diameters of the order of 200 μm, and saturates for larger droplets. The resulting enthalpy flux $Q_S + Q_L > 0$ vanishes for droplets with diameters $d < 100$ μm, and increases with d for larger droplets. DNS results also show that droplets reduce mean air velocity and temperature and increase relative humidity as compared to the droplet-free flow.

Plain Language Summary This study is concerned with numerical simulation of momentum, heat, and moisture exchange processes occuring in the marine atmospheric boundary layer. In particular, the influence of sea-spray drops on these processes is investigated. It is shown that drops reduce the mean air velocity and temperature, and increase relative humidity as compared to droplet-free flow.

1. Introduction

Detailed knowledge of momentum, heat, and mass transfer in the marine atmospheric boundary layer is necessary for correct parameterization of turbulent exchange processes at the air-sea interface in prognostic models. At sufficiently strong winds, sea-spray droplets also contribute to the transfer processes. The results of field experiments and laboratory measurements compiled by Andreas et al. (2010) show that the dominant contribution to the total water mass fraction in the near-surface air belongs to spume droplets. These droplets are torn off the surface wave crests at sufficiently strong winds, and their diameters are typically in the range of tens to hundreds of microns. Airborne droplets exchange momentum, heat, and moisture with the surrounding air via viscous drag force and diffusive heat and mass (vapor) fluxes (cf. e.g., Andreas, 1992; Borisenkov, 1974; Bortkovskii, 1973, 1987; Ling & Kao, 1976; Wu, 1974). Droplets-mediated momentum and sensible heat transfer is caused by a generally nonzero relative droplet-air velocity and temperature differences arising due to droplets inertia and different temperatures of air and seawater. The vapor exchange occurs due to droplets evaporation (or condensation) and is accompanied by the latent heat consumption (or release) by the droplets. This contributes to both the humidity of the surrounding air and the difference between the air and droplets temperatures (as discussed, e.g., by Pruppacher & Klett, 1978, and Andreas, 1989).

At present not all the details of spume droplets production mechanism are well understood. Recent findings of high-speed video-recording of spume droplets production in a laboratory study by Troitskaya et al. (2017)

and Troitskaya, Druzhinin, et al. (2018) indicate that at wind speeds exceeding 20 m/s, the dominant mechanism of spume droplets generation is that of a *bag-breakup* fragmentation. This fragmentation is somewhat similar to the well-known fragmentation of liquid droplets and jets in gaseous flows (see, e.g., Gelfand, 1996). The first evidence of this spray-production mechanism in a laboratory flume was reported by Veron et al. (2012). The fragmentation process starts with a small-scale elevation of the water surface which further develops into a *microsail* consisting of a water film bordered by a thicker rim (thus forming the *bag*). The bag is inflated by the wind and finally bursts and produces hundreds of droplets. Troitskaya et al. (2017) and Troitskaya, Druzhinin, et al. (2018) developed a statistical description of the bag-breakup phenomena, but the Probability Distribution Function (PDF) of the drops velocities at injection still remains unknown and requires further research.

The effects of spray on turbulent exchange processes in the marine atmospheric boundary layer have been extensively studied within the framework of phenomenological models (cf. e.g., Andreas & Emanuel, 2001; Bao et al., 2011; Fairall et al., 1994; Kudryavtsev, 2006; Kudryavtsev & Makin, 2011). These models use source functions introduced into the airflow Reynolds-averaged equations to account for feedback contributions by the droplets to the air mass and momentum fluxes. These feedback contributions are parameterized via bulk air flow properties such as 10-m wind speed, U_{10}, and air-sea-surface temperature and humidity difference. Parameterizations used in these models however require detailed knowledge of the droplets dynamics (which is considered as a subgrid process by these models) and usually rely on numerical simulations using Lagrangian stochastic approach (cf. e.g., Edson & Fairall, 1994; Mueller & Veron, 2014; Troitskaya et al., 2016).

Lagrangian stochastic models solve equations of the droplets motion in an airflow with prescribed velocity, temperature, and humidity fields. Thus, the air velocity, temperature, and humidity mean profiles are prescribed by a logarithmic boundary-layer approximation, whereas their fluctuation components are obtained as numerical solutions to Langevin equations with stochastic forcing. The properties of the forcing are chosen to mimic turbulent fluctuations of the airflow properties *seen* by droplets traveling through the atmospheric boundary layer in natural conditions. Lagrangian stochastic models provide very important information about droplets dynamics and can be used for estimates of droplets-mediated exchange of momentum, heat, and mass. However, it is recognized that these models are unable to reproduce the two-way interaction between the droplets and turbulent boundary-layer eddy structures (Mueller & Veron, 2014). The model definition of the properties of the airflow fields seen by the droplets is also problematic.

Richter and Sullivan (2013) were first who used direct numerical simulation (DNS) to model possible effects of sea-spray droplets on the marine boundary layer. These authors considered a turbulent Couette flow laden with solid particles over a *flat* surface as an idealized model of the atmospheric boundary layer and evaluated the momentum feedback effects due to the particles. The results show that particles may significantly reduce the carrier flow vertical turbulent momentum flux. The results also show that in the range of particle sizes similar to those of spume droplets typically found near the air-sea interface, particle inertial effects are significant and dominate any particle-induced stratification effects, considered to be of importance in phenomenological models (Kudryavtsev, 2006). In their later study, Richter and Sullivan (2014) considered the feedback effects of solid, nonevaporating particles on the vertical turbulent heat flux and found it to be significant. Thermodynamic coupling between evaporating particles/droplets and air and its influence on the sensible and latent heat fluxes were further studied by Helgans and Richter (2016) in a particle-laden turbulent Couette flow in zero-gravity environment and by Peng and Richter (2017) in a droplet-laden open channel flow with gravitational settling taken into account. The results of both studies show that evaporating droplets have opposite effects with regard to bulk sensible and latent heat transfer. Droplets that both respond rapidly to the ambient environment and have long suspension times are able to modify the latent and sensible heat fluxes individually, however the competing signs of this modification lead to an overall weak effect on the total heat flux. On the other hand, droplets with a slower thermodynamic response to the environment are less subjected to this compensating effect.

DNS of the droplet-laden turbulent Couette flow over a *waved* water surface was performed by Druzhinin et al. (2017). The results show that droplets dynamics and their impact on the carrier airflow is very sensitive to the droplets velocity at injection and also depends on the ratio of droplets gravitational settling velocity versus the product of air friction velocity and Karman constant ($V_g/\kappa u_*$), and the wave slope, *ka*. Note,

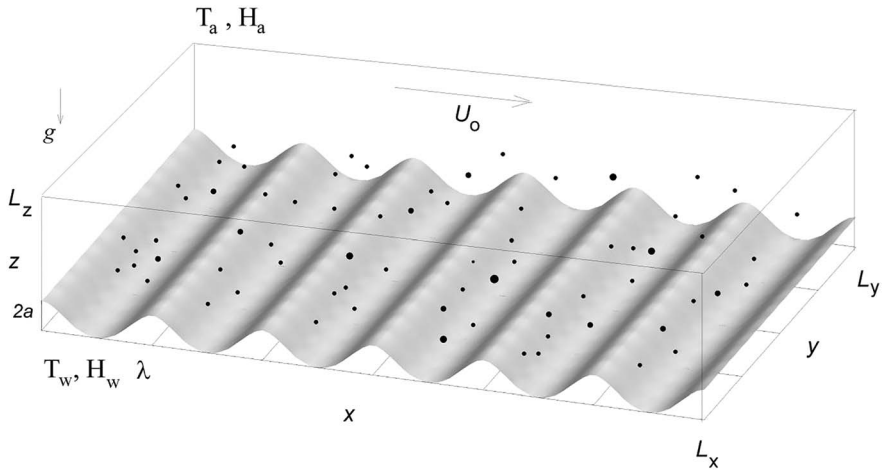

Figure 1. Schematic of numerical experiment: L_x, L_y, L_z are the domain sizes in the horizontal (x), spanwise (y), and vertical (z) directions; a and λ are the surface water wave amplitude and length; T_w, H_w and T_a, H_a are the temperature and fractional relative humidity at the water surface and at the top (air) boundary, respectively; U_0 is the bulk velocity of the airflow; and g is the acceleration due to gravity. Droplets are denoted by black dots. Symbols sizes are not to scale.

however, that Druzhinin et al. (2017) did not take into account droplets evaporation and heat exchange with the surrounding air which typically occur in natural conditions.

In the present paper, we perform DNS study of a droplet-laden Couette flow over waved water surface and take into account both drops-mediated momentum feedback and sensible and latent heat exchange with the carrier airflow. Turbulent Couette flow configuration in the present DNS is similar to that considered by Druzhinin et al. (2017). Evolution equations of the airflow velocity, temperature, and humidity are solved in a Eulerian framework simultaneously with the equations of individual droplets coordinates and velocities, temperatures, and masses tracked in a Lagrangian framework. The feedback effects of droplets on the airflow are modeled via a point-force approximation, and both momentum and latent and sensible heat exchange between droplets and air are taken into account. The evolution equations of the droplets masses and temperatures are formulated on the basis of droplets microphysics in clouds adapted for sea-spray conditions (Andreas, 1989; Pruppacher & Klett, 1978). The flow and droplets parameters in DNS are matched to typical known spume-droplets parameters in laboratory and field experiments documented in the literature. Section 2 below presents the governing equations and numerical method. Numerical results are discussed in section 3, and final conclusions and discussion are provided in section 4.

2. Governing Equations and Numerical Method

The schematic of DNS is similar to that considered by Druzhinin et al. (2017; Figure 1). A Cartesian framework is employed where x axis is oriented along the mean wind, z axis is directed vertically upward, and y axis is orthogonal to the mean flow and parallel to the wave front. We prescribe two-dimensional, x-periodic water wave with amplitude a, wavelength λ, and celerity c. The wave slope considered in our DNS is $ka = 2\pi a/\lambda = 0.2$. The rectangular computational domain has sizes $L_x = 6\lambda$, $L_y = 4\lambda$, and $L_z = \lambda$ in the x, y, and z directions, respectively, and the air flow is assumed to be periodic in the x and y directions. DNS is performed in a reference frame moving with the wave phase velocity, c, so that horizontal coordinate in the moving framework equals $x = x' - ct$, where x' is the coordinate in the laboratory reference frame. Thus, the bottom boundary representing the wave surface is stationary in the moving reference frame. No-slip boundary condition is prescribed for the air velocity at the bottom boundary, where it coincides with the velocity in the surface wave (to be specified below), and at the top boundary plane moving in the x direction with bulk velocity, U_0. The latter condition provides an external source of momentum due to viscous shear stress which compensates for viscous dissipation and makes the flow statistically stationary. Air and water surface temperatures and fractional relative humidity are prescribed, respectively, as T_w and H_w at the water surface and T_a and H_a at the top boundary plane, $z = L_z$. Typically $Tw > T_a$ and $H_w > H_a$.

The numerical algorithm is based on the integration of full, 3-D Navier-Stokes equations for the carrier airflow velocity and equations for the air temperature and relative humidity coupled with the equations for individual drops coordinates, velocities, temperatures, and masses. The equations for the air flow velocity, temperature, and relative humidity are written in the form (cf. e.g., Monin & Yaglom, 1971):

airflow momentum:

$$\frac{\partial U_i}{\partial t}+\frac{\partial\left(U_iU_j\right)}{\partial x_j}=-\frac{1}{\rho_a}\frac{\partial P}{\partial x_j}+\nu\frac{\partial^2 U_i}{\partial x_j\partial x_j}+\sum_{n=1}^{N_d} f_{Ui}^n, \tag{1}$$

continuity:

$$\frac{\partial U_j}{\partial x_j}=0, \tag{2}$$

air temperature:

$$\frac{\partial T}{\partial t}+\frac{\partial\left(TU_j\right)}{\partial x_j}=\kappa\frac{\partial^2 T}{\partial x_j\partial x_j}\sum_{n=1}^{N_d} f_T^n, \tag{3}$$

relative humidity:

$$\frac{\partial H}{\partial t}+\frac{\partial\left(HU_j\right)}{\partial x_j}=D\frac{\partial^2 H}{\partial x_j\partial x_j}+\sum_{n=1}^{N_d} f_H^n, \tag{4}$$

where $x_i=x,y,z$, $U_i(i=x,y,z)$ are the velocity components, P is pressure, ρ_a is the air density, T and H are instantaneous air temperature and fractional relative humidity, ν and κ are the air kinematic viscosity and thermal diffusivity, and D is the diffusivity of water vapor. Since the air-water temperature difference (T_w-T_a) considered in the present work is relatively insignificant (1 K), the air density, kinematic viscosity, and thermal diffusivity of air, molecular diffusivity of water vapor as well as saturated vapor density (when computing H), are evaluated at temperature T_a and atmospheric pressure P_a. Terms on the right hand side of equations (1), (3), and (4), f_{Ui}^n, f_T^n, and f_H^n, represent the feedback contributions (defined below) of nth droplet (n = 1, …, N_d) to the rate of change of air momentum, temperature, and humidity; N_d is the total, constant number of droplets considered in DNS. In the equation for the air momentum, equation (1), the buoyancy force is omitted since, under typical natural (cyclone) conditions, the Obukhov length scale typically far exceeds the height of the droplet-populated near-surface layer where the influence of the buoyancy force related to the air temperature gradient can thus be regarded negligible (cf. e.g., Kudryavtsev, 2006).

Spherical drops of diameter d_n, temperature T_n, and mass m_n (equal to $\rho_n\pi d_n^3/6$, where ρ_n is the salt solution density of the nth drop) are tracked in a Lagrangian framework. Thus, for each drop we solve equations for the coordinate, velocity, temperature (assumed to be uniform throughout the drop volume), and mass simultaneously with equations (1)–(4) (Bortkovskii, 1973, 1987):

drop coordinate:

$$\frac{dr_i^n}{dt}=V_i^n, \tag{5}$$

drop velocity:

$$\frac{dV_i^n}{dt}=\frac{1}{\tau_n}\left(U_i(r^n)-V_i^n\right)\left(1+0.15\,\mathrm{Re}_d^{0.687}\right)-\delta_{iz}\frac{V_s}{\tau_n}, \tag{6}$$

drop temperature:

$$m_n c_w \frac{dT_n}{dt} = 2\pi\kappa' d_n (T(r^n) - T_n)\left(1 + 0.25\,\mathrm{Re}_n^{0.5}\right) + L_v \frac{dm_n}{dt}, \tag{7}$$

drop mass:

$$\frac{dm_n}{dt} = 2\pi D' d_n \rho_{sat}^v \left(H(r^n) - H_n^s\right)\left(1 + 0.25\,\mathrm{Re}_n^{0.5}\right). \tag{8}$$

In equations (5)–(8), $r_i^n = x_n, y_n, z_n$ are Cartesian drop coordinates, and the full (Lagrangian) derivative over time (d/dt) is taken along the drop trajectory.

In equation (6), $U_i(r^n)$ is the instantaneous airflow velocity at the location of nth drop, V_s is the drop gravitational settling velocity (to be defined below), and τ_n is the drop response time,

$$\tau_n = \frac{d_n^2}{18\nu}\frac{\rho_n}{\rho_a}. \tag{9}$$

The drop velocity equation, equation (6), is written assuming that forces including air-pressure gradient, Basset, added-mass, and shear-induced Saffman's force, can be regarded negligible as compared to the viscous drag and gravity forces for the considered density ratio, $\rho_n/\rho_a \approx 10^3$ (Maxey & Riley, 1983). The correction of the viscous drag force on the drop by the surrounding air in equation (6) is introduced as in Clift et al. (1978), taking into account that particle Reynlods number, defined as

$$\mathrm{Re}_n = \frac{|U(r^n) - V^n| d_n}{\nu}, \tag{10}$$

is finite.

Equation (7) describes the rate of change of the drop temperature due to the sensible, diffusive heat flux from the surrounding air (the first term on the right hand side), and due to the latent heat flux (the second term on the right hand side) consumed (or released) by the drop evaporation (or condensation). The sensible heat flux is proportional to the product of the instantaneous difference of air temperature at the drop location, $T(r^n)$, and drop temperature, T_n, and thermal conductivity coefficient, κ' (not to be confused with the thermal diffusivity coefficient κ on the right hand side of equation (3)). Coefficient κ' is evaluated in DNS by the following approximation taking into account the noncontinuum gas-kinetic effects:

$$\kappa' = c_a \rho_a \kappa \left[\frac{d_n}{d_n + 2\Delta_T} + \frac{2\kappa}{\alpha_T d_n}\left(\frac{2\pi M_a}{R_g T(r^n)}\right)^{1/2}\right]^{-1}, \tag{11}$$

where c_a is the specific heat of air, M_a is the molecular weight of dry air, R_g is the universal gas constant, length scale, and dimensionless coefficient α_T = 0.7, as discussed by Pruppacher and Klett (1978) and Andreas (1989). When computing the heat flux we also take into account ventilation effects due to finite Reynolds number, Re_n, of the drop. The latent heat flux is proportional to the rate of change of droplet mass with the factor, L_v, the latent heat of vaporization (cf. Pruppacher & Klett, 1978).

Equation (8) describes the rate of change of the droplet mass. The right hand side of equation (8) includes the modified diffusivity of water vapor, D', the saturated vapor density, ρ_{sat}^v, and the difference between the surrounding relative humidity and relative humidity at the surface of the drop at saturation, H_n^s. These quantities are computed as follows (Andreas, 1989; Pruppacher & Klett, 1978):

modified diffusivity of water vapor:

$$D' = D\left[\frac{d_n}{d_n + 2\Delta_v} + \frac{2D}{\alpha_c d_n}\left(\frac{2\pi M_w}{R_g T_n}\right)^{1/2}\right]^{-1}, \tag{12}$$

where M_w is the molecular weight of water and dimensionless coefficient α_c = 0.036. Constant length scales, $\Delta_T = 2.17 \times 10^{-7}$m and $\Delta_v = 8 \times 10^{-8}$m, in equations (11) and (12) are related to the molecular mean free-path

and modify air thermal conductivity and molecular diffusivity of water vapor to account for noncontinuum gas-kinetic effects as discussed by Pruppacher and Klett (1978) and Andreas (1989);

saturated vapor density:

$$\rho_{sat}^{v} = \frac{M_w e_s[T(r^n)]}{R_g T(r^n)}, \tag{13}$$

where the saturated vapor pressure at temperature T, $e_s(T)$, is evaluated by employing the approximation introduced by Buck (1981; cf. also Andreas, 1989);

relative humidity at the droplet surface at saturation:

$$H_n^s = \frac{T_a(r^n)}{T_n} \exp\left[L_v M_w \frac{T_n - T(r^n)}{T_n T(r^n)} + \frac{4\sigma M_w T(r^n)}{d_n \rho_w R_g T_n} - \frac{2\Phi m_{ns} M_w}{M_s(m_n - m_{ns})}\right], \tag{14}$$

where σ is the surface tension of a flat surface of water with the same salinity and temperature as the droplet solution; Φ is the practical osmotic coefficient of the drop; M_s is the molecular weight of salt; ρ_w is the fresh water density; and m_{ns} is a mass of salt in the nth drop. The latter remains constant for each drop during simulation and is defined by the initially prescribed salinity of sea water (34 psu) and droplet volume (cf. Andreas, 1989).

The integration of equations (1)–(4) is performed in curvilinear coordinates (ξ, y, η) which are related to the Cartesian coordinates (x, y, z) as (Druzhinin et al., 2017)

$$x = \xi - a\exp(-k\eta)\sin k\xi, \tag{15}$$

$$z = \eta + a\exp(-k\eta)\cos k\xi. \tag{16}$$

This mapping, equations (15) and (16), transforms the lower wavy boundary, $z_s(x) = a\cos k\xi(x)$ (which up to $O(k^2a^3)$ coincides with an asymptotic solution for the Stokes wave, cf. Gent & Taylor, 1976), into a plane boundary at $\eta = 0$. The instantaneous airflow velocity, temperature, and relative humidity at the location of nth droplet, $U_i(r^n), T(r^n)$ and $H(r^n)$, are evaluated by a fourth-order Hermitian interpolation method (cf. e.g., Balachandar & Maxey, 1989) after mapping, equations (17) and (18), the droplet Cartesian coordinates onto curvilinear coordinates.

Equations (1)–(4) are discretized in a rectangular domain with sizes $0 < x < 6\lambda$, $0 < y < 4\lambda$, and $0 < z < \lambda$ by employing a finite difference Adams-Bashforth method of second-order accuracy on a uniform staggered grid consisting of 360 × 240 × 180 nodes. An additional mapping is employed to compress the grid nodes in the vertical direction near boundaries in order to resolve small-scale air motions (Druzhinin et al., 2012). Thus, the grid mesh size equals $\Delta x/\lambda = 1/60$ in the streamwise and spanwise directions, whereas in the vertical direction the mesh size increases from $\Delta z_1/\lambda \approx 0.0008$ near the walls to $\Delta z_2/\lambda \approx 0.009$ in the middle of computational domain. When normalized by the wall scale, ν/u_*, the mesh sizes for the considered Re are found to be equal to $\Delta x^+ \approx 6$ in the horizontal plane and varying from $\Delta z_1^+ \approx 0.3$ near boundaries to $\Delta z_2^+ \approx 3$ in the middle of the domain. Comparable mesh sizes were used in DNS studies by Sullivan et al. (2000) and Yang and Shen (2010). The Poisson equation for the pressure is solved by iterations. Numerical method of integration of equations (1)–(4) used in the present study is quite similar to that employed in both droplet-free and droplet-laden cases by Druzhinin et al. (2012, 2017). In the latter case, we validated our numerical code by comparison with both available laboratory data and DNS results by Sullivan et al. (2000).

The airflow bulk Reynolds number in DNS is defined as

$$\mathrm{Re} = \frac{U_0\lambda}{\nu_a}, \tag{17}$$

and set equal to Re = 15,000. The corresponding friction Reynolds number is $\mathrm{Re}_* = u_*\lambda/\nu_a \approx 500$, where u_* is the airflow friction velocity (defined below). The wave-slope equals $ka = 0.2$. We prescribe the wave celerity to

be sufficiently small, $c/U_0 = 0.05$, which corresponds to *slow* waves as compared to the wind (cf. e.g., Sullivan et al., 2000; Yang & Shen, 2010). When prescribing the air temperature (measured in Kelvins, K) and fractional relative humidity at the waved surface and upper boundary, we take $T_a = 27 + T_k$(K) and $T_w = 28 + T_k$(K) (where $T_k = 273.15$ K), and $H_w = 0.98$ and $H_a = 0.8$, considered by Andreas and Emanuel (2001). It should be emphasized, however, that the Reynolds number considered in our DNS is far below the one observed in natural conditions. Thus, the air bulk velocity (analogous to the characteristic, U_{10}, velocity in natural experiment) is of the order of a few meters per second, and the friction velocity (u_*, of the order of 10 cm/s) is much smaller than its natural counterpart. Thus, the present study can be regarded only as a scaled mathematical model.

At the lower-plane boundary ($\eta = 0$) the no-slip (Dirichlet) conditions for the air velocity, temperature, and relative humidity are prescribed. The airflow velocity here coincides with the velocity of the water in the surface wave:

$$U_x(\xi, y) = c(ka\cos kx(\xi, \eta) - 1), \tag{18}$$

$$U_y(\xi, y) = 0, \tag{19}$$

$$U_z(\xi, y) = cka\sin kx(\xi, \eta). \tag{20}$$

At the upper boundary ($\eta/\lambda = 1$) the no-slip condition for the wind velocity is prescribed with respect to the plane moving with nondimensional velocity $(1 - c)$:

$$U_x(\xi, y) = 1 - c, \tag{21}$$

$$U_y(\xi, y) = 0, \tag{22}$$

$$U_z(\xi, y) = 0. \tag{23}$$

The air temperature and relative humidity deviations from the respective boundary values, $T_{a,w}$ and $H_{a,w}$, are set equal to zero at both the waved surface and the upper boundary. Periodic boundary conditions are prescribed for all fields at the side boundaries of the computational domain, namely, at $\xi/\lambda = 0$, 6 and $y/\lambda = 0$, 4.

The equations for drops coordinates, velocities, masses, and temperatures, equations (5)–(8), are integrated in the Cartesian framework with the use of a second-order Adams method for the coordinate, equation (3), and the Adams-Bashforth method for the velocity, equation (4). The inverse transform from the Cartesian to curvilinear drops coordinates is performed by an iterative Newton's method (Druzhinin et al., 2017). Note that in the present study, we perform the integration of the equation (8) for the drop mass and do not employ the equation for the drop diameter, d_n. This equation can be directly derived from equation (8) and shows that $d(d_n)/dt \sim d_n^{-2}$ which makes the integration problematic for small d_n (cf. Andreas, 1989). Thus, at each time step, the new drop mass and temperature are obtained, $m_n(t + \Delta t)$ and $T_n(t + \Delta t)$. The mass of pure water evaporated from the drop is further obtained as $\Delta m_n(t) = m_n(t + \Delta t) - m_n(t)$. This gives the change of the drop volume, $\pi\Delta d_n^3/6 = \Delta m_n/\rho_w$, where ρ_w is the density of pure water defined for given $T_n(t)$ and atmospheric pressure (P_a = 1,000 mb). (Note that both Δm and Δd are negative if the drop evaporates.) Thus, the drop new diameter is defined as $d_n(t + \Delta t) = d_n(t) + \Delta d_n$, and the new drop solution density is found as $\rho_n(t + \Delta t) = \pi d_n^3(t + \Delta t)/6m_n(t + \Delta t)$. The numerical method performance was verified by a comparison with the results of integration of the full microphysical model equations by employing the numerical algorithm developed by Andreas (2013).

The feedback contributions of each drop to the rate of change of air flow momentum, temperature, and moisture, f_{Ui}^n, f_T^n, and f_H^n, on the right hand side of equations (1), (3), and (4) are formulated with the use

of a point-force approximation. Thus, the contributions by nth droplet are evaluated by distributing them to the nearest eight grid nodes surrounding the drop in the form (Druzhinin, 2001; Druzhinin et al., 2017):

$$f_{Ui}^{n} = \frac{\pi d_n^3}{6}\frac{\rho_d^n}{\rho_a}\frac{1}{\tau_n}\left(V_i^n - U_i(r^n)\right)\left(1 + 0.15\,\mathrm{Re}_n^{0.687}\right)\frac{w(r^n, r)}{\Omega_g}, \tag{24}$$

$$f_{T}^{n} = 2\pi\kappa' d_n(T_n - T_a(r^n))\left(1 + 0.25\,\mathrm{Re}_n^{0.5}\right)\frac{1}{\rho_a c_a}\frac{w(r^n, r)}{\Omega_g}, \tag{25}$$

$$f_{H}^{n} = -\frac{1}{\rho_{sat}^{v}}\frac{dm_n}{dt}\frac{w(r^n, r)}{\Omega_g}, \tag{26}$$

where $w(r^n, r)$ is a geometrical weight-factor inversely proportional to the distance between nth drop located at $r^n = (x^n, y^n, z^n)$ and the grid node located at $r = (x, y, z)$, and Ω_g (r) is the volume of the considered grid cell. Thus, for each individual drop, eight weight-factors are defined (for each of the surrounding grid nodes) and normalized so that the sum of partial feedback contributions distributed to these nodes exactly equals the respective total feedback contribution. Therefore, there is no numerically induced loss or gain of momentum, heat, and moisture in the drops-air exchange processes.

In the present study, we aim at modeling the details of spray-mediated heat, mass, and momentum exchange processes occurring in the marine atmospheric boundary layer. Experimental data compiled by Andreas et al. (2010) show that the dominant contribution, with regard to the mass fraction, typically belongs to spume drops with diameters around 200 μm. As is also known from observations, for these drops the ratio of the terminal settling velocity, $V_s = \tau_g$ (where g is the gravitational acceleration and the drop response time, τ, is given by equation (11)), versus the product of the Karman constant and the friction velocity, κu_*, is of the order of unity. This ratio ($V_s/\kappa u_*$) indicates whether gravitational settling of the drops is important as compared to the advection by turbulent eddies in the boundary layer (cf. Andreas et al., 2010). The settling velocity of a 200-μm drop in still air is about 60 cm/s (Andreas, 1989). Therefore, the droplet of this size can be regarded as suspended in the air for the friction velocity of more than 1 m/s. The dimensional friction velocity in present DNS is about 10 times smaller, so we adjust our mathematical model to the natural situation, with regard to the drops dynamics, by proportionally reducing the gravitational acceleration. This reduction does not affect the feedback momentum and heat fluxes but makes the residence times of drops considered in DNS (based on the ratio $V_s/\kappa u_*$) similar to the adopted estimates of residence times of spume drops in the air in natural conditions. Similar reduced-gravity conditions were considered by Peng and Richter (2017) in the DNS study of droplet-laden open channel flow modeling MABL.

Therefore, the droplets are injected with random ratio ($V_s/\kappa u_*$) distributed uniformly in the range $0.25 \le V_s/\kappa u_* \le 2.25$. Thus, the equivalent dimensional droplets diameters at injection, $d(t_{inj}) \equiv d_0$, are distributed in the range $100\ \mathrm{m\mu} \le d_0 \le 300$ μm. Unfortunately, at present there are no published accurate measurements of the near-surface sea-spray drops concentration under strong wind forcing in natural conditions. The droplets mass fraction considered in present DNS equals $C_m \approx 0.038$ and is prescribed so as to make the feedback effects of droplets upon the carrier flow significant enough (i.e., noticeable) whereas to keep their volume fraction sufficiently small (far below 10^{-4}) in order to neglect the hydrodynamic interactions between neighboring droplets. Creating this *initial*, uniformly distributed mass fraction requires tracking $N_d = 3 \cdot 10^6$ droplets.

If a droplet leaves the computational domain via a side boundary plane, it reenters the domain at the respective opposite side boundary with the same z coordinate and velocity due to periodicity in x and y directions. If the droplet either reaches the bottom boundary plane (the water surface, $\eta = 0$) or the upper horizontal moving plane (at $\eta/\lambda = 1$) it is reinjected into the flow.

Natural and laboratory observations show that spume drops are typically formed in the vicinity of the wave crests (Andreas et al., 2010; Fairall et al., 2009). The latest results of high-speed video recording in laboratory experiments by Troitskaya et al. (2017) and Troitskaya, Druzhinin, et al. (2018) testify that the so-called bag-breakup fragmentation taking place at the wave crests is mainly responsible for spume drops production. The drops injection above wave crests was also employed in Lagrangian stochastic models (cf. Mueller & Veron, 2014; Troitskaya et al., 2016) and in recent DNS by Druzhinin et al. (2017). Thus, in present DNS, the

drops are injected at distance $0.01 < \eta/\lambda < 0.05$ ($5 < \eta u_*/\nu < 25$) from the water surface (in the buffer layer) at random locations at the upwind wave slopes in the vicinity of the wave crests (within region $m\lambda - 0.2 < \xi < m\lambda$, $m = 1, \ldots, 6$). Since the drops velocity distribution at injection is yet unknown, we adopt a scenario considered by Andreas and Emanuel (2001) and Andreas (2004). Under this scenario, the droplets are *torn off* the wave crests and thus have initial velocities equal to those of water particles in the surface wave. These velocities are evaluated from equations (15) and (16) for a given $x(\xi, \eta)$ coordinate of each drop at injection. The droplets temperatures at injection are prescribed to be equal to the water surface temperature, T_w.

The air velocity field is initiated as a weakly perturbed laminar Couette flow, and the initial deviations of temperature and relative humidity profiles from respective linear reference profiles,

$$T_{ref}(z) = T_w + (T_a - T_w)\frac{z}{\lambda}, \tag{27}$$

$$H_{ref}(z) = H_w + (H_a - H_w)\frac{z}{\lambda}, \tag{28}$$

are set equal to zero. During an initial transient, $0 < tU_0/\lambda < 100$, the feedback forces due to drops at the right hand side of equations (1), (3), and (4) are put to zero, and a fully developed turbulent, unladen flow regime sets in. At time $tU_0/\lambda = 100$, droplets are introduced into the flow uniformly at random locations with random ratio $V_g/\kappa u_*$ as discussed above. Their initial velocities and temperatures are set equal to those of the surrounding air. The initial diameter and mass of salt in each drop solution are stored and reassigned at further reinjections. The equations of motion of air and droplets, equations (1)–(4) and (5)–(8), are solved simultaneously during time interval $100 < tU_0/\lambda < 150$ with the feedback forces *turned off*. During this transient, the drops dynamics adjust to the airflow dynamics. At later times, $150 < tU_0/\lambda < 200$, the airflow and drops equations of motion are solved with the feedback forces *turned on*. During this time interval, a statistically stationary, droplet-laden, two-way-coupled flow regime is established. Statistical sampling of the air flow and drops is performed during time interval $200 < tU_0/\lambda < 300$ at discrete time moments t_k $(k = 1, \ldots, 500)$ with increments $t_{k+1} - t_k = 0.2\lambda/U_0$. We also track several individual droplets with a much smaller sampling increment $(0.006\lambda/U_0)$ for elucidating the details of the momentum, heat, and mass exchange processes occurring between these drops and the surrounding air.

Similarly to the previous studies of airflow over waved surfaces by Sullivan et al. (2000), Yang and Shen (2010), and Druzhinin et al. (2012, 2017), in statistical postprocessing analysis we perform *phase* averaging, equivalent to averaging over an ensemble of turbulent fluctuations. This averaging is performed over y coordinate, time, and window-averaged over wave length and denoted by angular brackets:

$$\langle F\rangle(\xi,\eta) = \frac{1}{6N_tN_y}\sum_{j=1}^{N_y}\sum_{k=1}^{N_t}\sum_{n=0}^{5} F\left(\xi + n\lambda, y_j, \eta, t_k\right), \tag{29}$$

$$\left\langle F^2\right\rangle(\xi,\eta) = \frac{1}{6N_tN_y}\sum_{j=1}^{N_y}\sum_{k=1}^{N_t}\sum_{n=0}^{5} F^2\left(\xi + n\lambda, y_j, \eta, t_k\right), \tag{30}$$

where F stands for air velocity components, temperature, and humidity fields; $N_y = 240$, $N_t = 500$, and $0 < \xi < 1$. The dispersion of F is further obtained in the form:

$$F'^2 = \left\langle F^2\right\rangle - \langle F\rangle^2. \tag{31}$$

We also introduce rectangular brackets for the *mean* vertical profile, $[F](\eta)$, obtained by additional averaging of $\langle F\rangle(\xi,\eta)$ along the streamwise coordinate:

$$[F](\eta) = \frac{6}{N_x}\sum_{k=1}^{N_x/6}\langle F\rangle(\xi_k,\eta), \tag{32}$$

where $N_x = 360$. The RMS fluctuation of F is obtained as

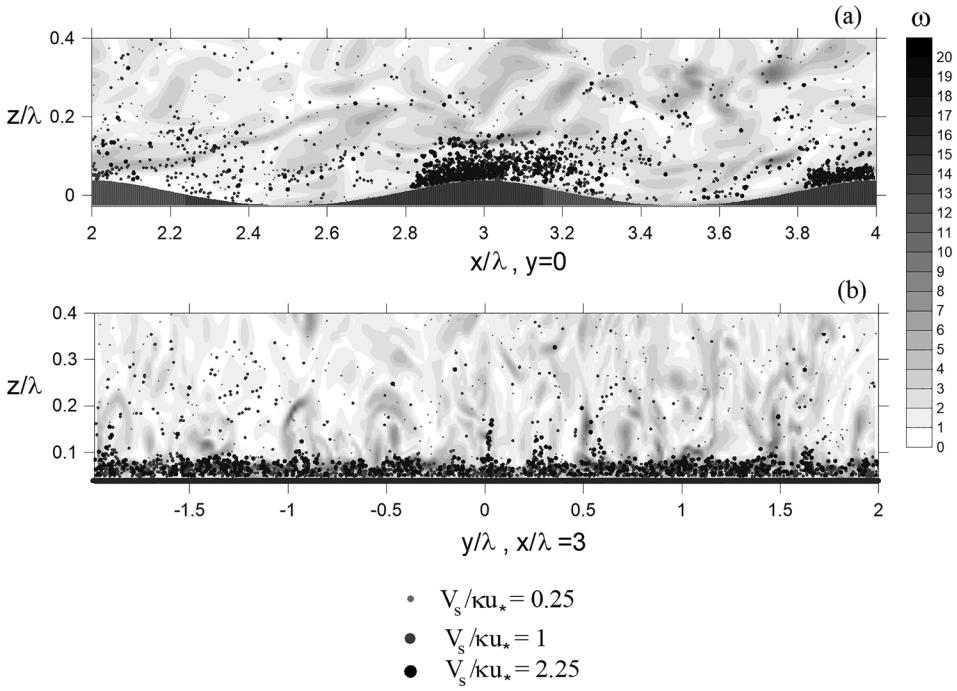

Figure 2. Instantaneous distribution of the vorticity modulus, ω (gray scale), and droplets locations (symbols) in DNS at $tU_0/\lambda = 300$ in central (x,z) (a) and (y,z) (b) planes. Only the droplets with the ratio $V_s/\kappa u_* \approx 0.25$ (for droplets with diameter $d \approx 100\mu$m), $V_s/\kappa u_* \approx 1$ ($d \approx 200\mu$m), and $V_s/\kappa u_* \approx 2.25$($d \approx 300\mu$m) (represented by symbols of different color and size) are shown. Symbols sizes are not to scale. Here and below wave slope $ka = 0.2$.

$$\left[F'\right](\eta) = \left\{\frac{6}{N_x}\sum_{k=1}^{N_x/6} F'^2(\xi_k,\eta)\right\}^{1/2}. \tag{33}$$

Phase-averaged vertical profiles of turbulent fluxes of air momentum, heat, and humidity are also determined, respectively, as

$$\tau_m(\xi,\eta) = \langle U_x\rangle\langle U_z\rangle - \langle U_x U_z\rangle, \tag{34}$$

$$\tau_T(\xi,\eta) = \langle T\rangle\langle U_z\rangle - \langle T U_z\rangle, \tag{35}$$

$$\tau_H(\xi,\eta) = \langle H\rangle\langle U_z\rangle - \langle H U_z\rangle, \tag{36}$$

and mean vertical profiles of the fluxes, $[\tau_m](\eta)$, $[\tau_T](\eta)$, and $[\tau_H](\eta)$, are obtained by averaging of equations (34)–(36) over ξ as in equation (32). The friction velocity, u_*, can be defined as

$$u_* = \left[\tau_m\right]^{1/2}\Big|_{\eta=0.5\lambda}, \tag{37}$$

where the contribution of the wave-induced momentum flux is negligible (cf. a discussion by Druzhinin et al., 2016, 2017).

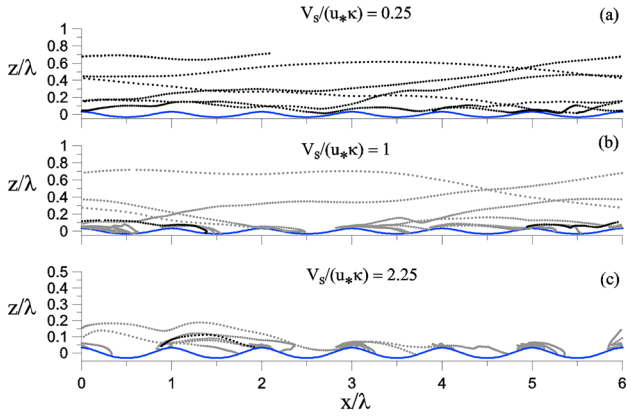

Figure 3. The side view of the trajectories of droplets injected with different diameters and ratio $V_s/(\kappa u_*)$ at injection: (a) $V_s/(\kappa u_*) \approx 0.25$ ($d \approx 100\mu$m); (b) ($d \approx 200\mu$m); and (c) $V_s/(\kappa u_*) \approx 2.25$ $d \approx 300\mu$m).The trajectories obtained during the total simulation time ($100 \le tU_0/\lambda \le 300$) are shown in gray color. The trajectories selected for droplets dynamics analysis (in Figures 4–6 below) are shown in black color.

3. Numerical Results

3.1. Instantaneous Distribution and Lagrangian Dynamics of Drops

Figures 2 and 3 demonstrate how the drops sizes affect its dynamics and distribution. Figure 2 shows the instantaneous distribution of the flow vorticity modulus field and drops locations obtained in DNS at time $tU_0/$

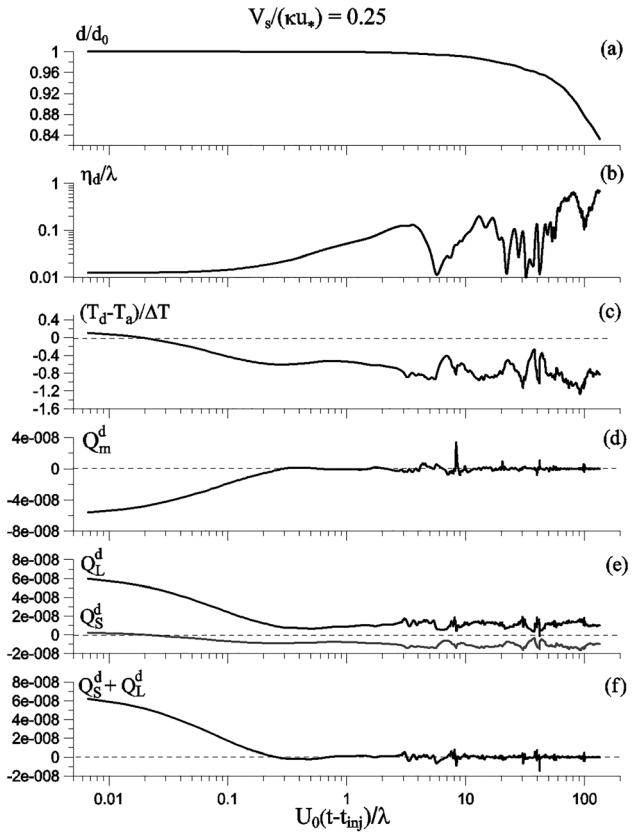

Figure 4. Temporal development of the instantaneous droplet diameter (a); height above the water surface (b); difference between droplet temperature and surrounding air temperature (c); momentum flux from the droplet to the surrounding air, Q_m (d); sensible and latent heat fluxes from the droplet to the surrounding air, Q_S and Q_L (e); and the enthalpy flux ($Q_S + Q_L$) (f). Initial ratio $V_s/(\kappa u^*) \approx 0.25$ ($d \approx 100$ mμ).

$\lambda = 300$ in central (x,z) and (y,z) planes. For a better view we divided the drops into three categories: small drops with ratio $V_s/\kappa u_* \approx 0.25$ ($d \approx 100\mu$m); intermediate-size drops with $V_s/\kappa u_* \approx 1$($d \approx 200\mu$m); and large drops with $V_s/\kappa u_* \approx 2.25$ ($d \approx 300$mμ). The figure shows that the smallest drops are transported by turbulent eddies throughout the flow domain, whereas the largest drops locations are confined to the vicinity of the wave crests due to gravitational settling.

Figure 3 presents a side view of the trajectories of drops with different ratio $V_s/\kappa u_*$ at injection: cases (a) $V_s/(\kappa u_*) = 0.25$ ($d \approx 100\mu$m); (b) $V_s/(\kappa u_*) = 1$ ($d \approx 200\mu$m); (c) and $V_s/(\kappa u_*) = 2.25$ ($d \approx 300\mu$m), obtained in DNS with wave slope $ka = 0.2$. The trajectories obtained during the total simulation time ($100 \le tU_0/\lambda \le 300$) in cases (b) and (c) are shown in gray symbols, whereas trajectories selected for the analysis of drop-mediated momentum, sensible, and latent heat fluxes (discussed below in Figures 4–6) are shown in black symbols. The figure shows that a relatively small drop [case (a)], once injected, travels throughout the domain over many wavelengths without falling back into the water. On the other hand, motion of the largest drop, in case (c), is mostly confined to a near-water-surface layer at $z/\lambda < 0.1$. In the latter case, the drop injected above the upwind side of the surface wave typically travels about one wavelength in the streamwise direction and falls back into the water, either at the lee-side of the wave crest or in the vicinity of the wave trough.

We sampled various characteristics of the drops dynamics along the selected trajectories in Figure 3 (black symbols) with different $V_s/\kappa u_*$ (Figures 4–6): (a) the instantaneous droplet diameter normalized by the diameter at injection, (b) height above the water surface, and (c) the difference between the droplet temperature and the surrounding air temperature normalized by the water-air temperature difference; the fluxes of (d) momentum (Q_m^d), and (e) sensible (Q_S^d) and latent (Q_L^d) heat; and (f) the resulting enthalpy flux ($Q_S^d + Q_L^d$) from the drop to the surrounding air. (Here and below the fluxes are made dimensionless via normalizing by the bulk quantities.) Note that some features of the droplets behavior in Figures 4–6 are individual (e.g., instantaneous variations of droplet temperature and height above water, as well as observed local peaks of the momentum and heat fluxes). Nevertheless, there are common features typical of droplets with the same size (measured by the ratio $V_s/\kappa u_*$). These common features of the behavior of droplets with specified ratio $V_s/\kappa u_*$ are discussed below.

For the discussion to follow it is convenient to rewrite equations (8) and (9) for the x component of drop momentum and the drop temperature in the form

$$m_d \frac{dV_x^d}{dt} = -Q_m^d, \tag{38}$$

$$m_d c_w \frac{dT_d}{dt} = -Q_S^d - Q_L^d, \tag{39}$$

where the fluxes of momentum and sensible and latent heat from the drop to the surrounding air, Q_m^d, Q_S^d, and Q_L^d, are given by

$$Q_m^d = 3\rho_a \pi d\nu \left(V_x^d - U_x\left(r^d\right)\right)\left(1 + 0.15\,\mathrm{Re}_d^{0.687}\right), \tag{40}$$

$$Q_S^d = 2\pi\kappa' d\left(T_d - T_a\left(r^d\right)\right)\left(1 + 0.25\,\mathrm{Re}_d^{0.5}\right), \tag{41}$$

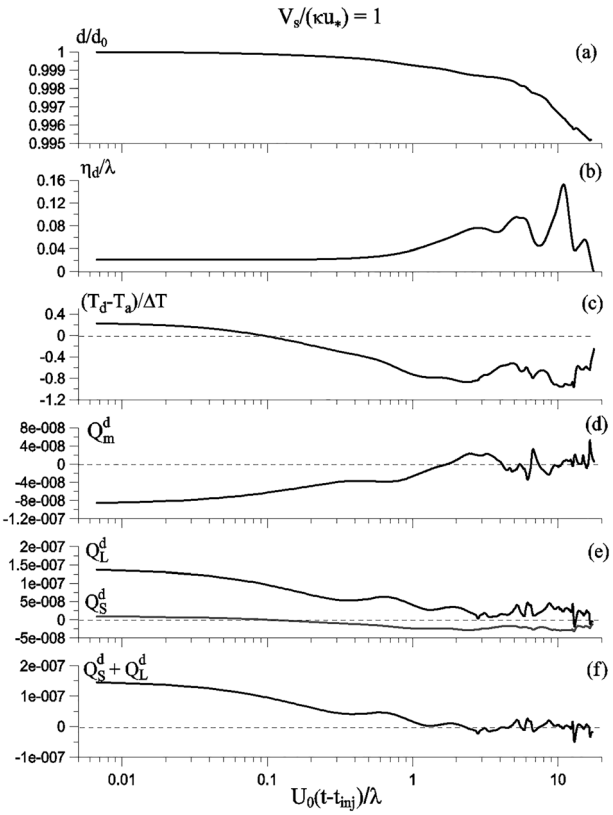

Figure 5. The same as in Figure 4 but for the drop with initial ratio $V_s/(\kappa u_*) \approx 1$ ($d \approx 200\mu m$).

$$Q_L^d = -L_v \frac{dm_d}{dt} = 2L_v \pi D' d\rho_{sat}^v \left(H_d^s - H\left(r^d\right)\right)\left(1 + 0.25\,\mathrm{Re}_d^{0.5}\right). \quad (42)$$

In equations (38)–(42), the drop mass equals $m_d = \rho_d \pi d^3/6$, and r^d and Re_d are the drop coordinate and Reynolds number, respectively. Other notations are the same as in equations (8)–(16).

As Figure 4 demonstrates, the drop with $V_s/\kappa u_* \approx 0.25$ ($d_0 \approx 100\mu m$) resides in the vicinity of the water surface (in the considered case, at $\eta_d/\lambda < 0.05$, or, in wall-scale normalized units, at $\eta_d u_* \mathrm{Re} < 20$, i.e., in the viscous sublayer and the buffer region of the boundary layer) at times $U_0(t - t_{inj})/\lambda < 1$ and is transported above the near-surface layer and travels throughout the domain at times $U_0(t - t_{inj})/\lambda > 1$ (cf. Figure 4b). Immediately after injection, the drop temperature is slightly higher as compared to the surrounding air ($(T_d - T_a)/\Delta T \approx 0.17$), and decreases due to evaporation and diffusion until it reaches an equilibrium temperature, T_d^{eq}, ($\left(T_d^{eq} - T_a\right)/\Delta T \approx -0.6$) at times $0.2 < U_0(t - t_{inj})/\lambda < 1$ (cf. Figure 4c). It is easy to show that the same equilibrium temperature ($T_d^{eq} \approx 27.1°C$) is predicted by the numerical model developed by Andreas (1989) if we substitute for bulk quantities considered in the model the air temperature and relative humidity at the given drop location above the water surface in present DNS (i.e., the drop initial temperature $T_w = 28°C$, air temperature $T_a \approx 27.7°C$, and relative humidity $H \approx 0.94$ at height $\eta_d/\lambda \approx 0.03$). Figure 4c also shows that the drop temperature fluctuates significantly as the drop travels throughout the domain. For the considered ratio of $V_s/\kappa u_* \approx 0.25$, the drop settling velocity is relatively small as compared to the turbulent air velocity, and the drop remains suspended in the air for a considerable time and does not fall back into the water until the end of the simulation when its diameter is substantially reduced (by about 20%) due to evaporation (cf. Figure 4a).

Figures 4d–4f present the behavior of momentum (Q_m^d, equation (37)) and sensible and latent heat fluxes (Q_S^d and Q_L^d, equations (41) and (42)), and the resulting enthalpy flux (i.e., the sum Q_S^d+Q_L^d) along the drop trajectory. As can be deduced from Figure 4d, the drop takes away momentum from the air (since $Q_m^d < 0$) immediately after injection, at times $U_0(t - t_{inj})/\lambda < 0.3$, as the drop is accelerated to the surrounding air velocity by the drag force. At later times, the drop velocity is mostly in equilibrium with the surrounding air velocity (so that $Q_m^d \approx 0$) with occasional fluctuations caused by intermittent turbulent eddies.

Immediately after injection (at times $U_0(t - t_{inj})/\lambda < 0.02$), both sensible ($Q_S^d$) and latent ($Q_L^d$) heat fluxes are positive, and Q_L^d exceeds Q_S^d by almost two orders of magnitude. Since the drop temperature decreases below the surrounding air temperature due to evaporation, the sensible heat flux becomes negative at times $U_0(t - t_{inj})/\lambda > 0.02$. The latent heat flux, Q_S^d, also decreases and at times $U_0(t - t_{inj})/\lambda > 0.2$ the drop enters a *wet bulb* state where its temperature is close to the equilibrium temperature, $T_d \approx T_d^{eq}$. In that state, the latent heat consumed by the drop evaporation is compensated by the sensible heat flux supplied via thermal diffusion from the surrounding air (Andreas, 1995):

$$Q_S^d + Q_L^d \approx 0. \quad (43)$$

As Figure 4e demonstrates, the balance, equation (43), holds after the initial transient at times $U_0(t - t_{inj})/\lambda < 0.2$ until the end of the simulation. As a result, the enthalpy flux (the sum of Q_L^d and Q_S^d) is positive immediately after injection, further decreases and finally vanishes at times $U_0(t - t_{inj})/\lambda > 0.2$ (Figure 4f).

Temporal behavior of the diameter and temperature and the feedback fluxes of the drop with ratio $V_s/\kappa u_* \approx 1$ (diameter $d \approx 200\mu m$) are qualitatively similar to those of the drop with $V_s/\kappa u_* \approx 0.25$($d \approx 100\mu m$): immediately after injection, d and T_d decrease due to evaporation, the momentum flux, Q_m^d, is negative, and both sensible and latent heat fluxes, Q_S^d and Q_L^d, are positive, and Q_L^d far exceeds Q_S^d(cf. Figure 5). At later times,

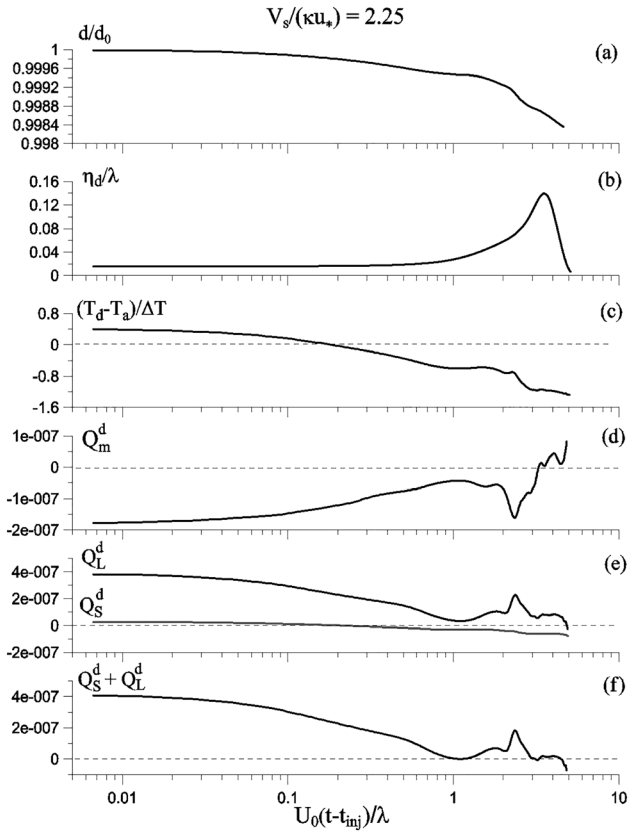

Figure 6. The same as in Figure 4 but for the drop with initial ratio $V_s/(\kappa u_*) \approx 2.25$ ($d \approx 300\mathrm{m}\mu$).

the drop is in equilibrium with the surrounding air velocity (since Q_m^d fluctuates near zero), and in the wet bulb state since Q_S^d is negative and Q_L^d is positive, and the enthalpy flux is near zero. However, since the drop settling velocity in this case is larger, the drop residence time in the air is finite (about $17\lambda/U_0$). The rate of change of the drop diameter, temperature, and velocity is also reduced, and the drop reaches the equilibrium wet bulb state at later times (at $U_0(t - t_{inj})/\lambda > 1$) as compared to the case $d = 100\mu\mathrm{m}$. The drop temperature decreases after injection and becomes lower than the air temperature, and $Q_S^d < 0$, at times $U_0(t - t_{inj})/\lambda > 0.1$ (Figure 5c).

The dynamics of the largest drop in Figure 3 with ratio $V_s/\kappa u_* \approx 2.25$ ($d \approx 300\mu m$), case (c), is dominated by gravitational settling and mostly consists of downwind advection of the drop after injection and its subsequent fall into the water in the vicinity of the neighboring wave crest (cf. black symbols in Figure 3c). As Figure 6d demonstrates, the drop extracts momentum from the air ($Q_m^d < 0$) during acceleration by the wind after injection, at times $U_0(t - t_{inj})/\lambda < 3$, and gives back a portion of its momentum to the air during its descent toward the water surface when Q_m^d becomes positive. Temperature T_d decreases due to evaporation below the surrounding air temperature after injection (and sensible heat flux, Q_S^d, decreases and becomes negative) at times $U_0(t - t_{inj})/\lambda > 0.2$, and attains equilibrium, $T_d \approx T_d^{eq}$, at $U_0(t - t_{inj})/\lambda \approx 1$. The latent heat flux is positive and much larger than the sensible heat flux, $Q_L^d \gg Q_S^d$, immediately after injection, but decreases and becomes of the order of Q_S^d as the drop enters the wet bulb state. In the considered case, the drop residence time in the air, as well as the duration of the equilibrium state, is rather short since the drop falls back into the water at $U_0(t - t_{inj})/\lambda \approx 5.3$. Figure 6 shows that as the drop descends toward the water surface, its temperature becomes significantly lower than the surrounding air temperature, whereas relative humidity of the surrounding air, H, increases. Under these conditions, the relative humidity at the surface of the drop at saturation, H_n^s, equation (16), decreases and becomes close to H, so the drop evaporation rate decreases and, consequently, Q_L^d is reduced. So during time interval $5 < U_0(t - t_{inj})/\lambda > 5.3$ both sensible and the resulting enthalpy fluxes are negative.

3.2. Drops Mean Distribution and Feedback Fluxes

Phase-averaged fields of the drops volume fraction (or concentration), $\langle C \rangle$, and the drops-mediated fluxes of momentum and sensible and latent heat per unit volume, $\langle Q_m \rangle$, $\langle Q_S \rangle$, and $\langle Q_L \rangle$, were evaluated by substitution in equation (29) the following respective quantities:

$$C = \frac{\pi d^3}{6} \sum_{m=1}^{N_d} \frac{w(r^m, r)}{\Omega_g}, \tag{44}$$

$$Q_m = \sum_{n=1}^{N_d} f_{Ux}^n, \tag{45}$$

$$Q_S = \sum_{n=1}^{N_d} c_a \rho_a f_T^n, \tag{46}$$

$$Q_L = -\sum_{n=1}^{N_d} L_v \rho_{sat}^v f_H^n, \tag{47}$$

where the feedback contributions of nth drop to the rate of change of air flow momentum, temperature, and moisture, f_{Ux}^n, f_T^n, and f_H^n, are defined in equations (26)–(28). Figure 7 presents distributions of $\langle C \rangle$, $\langle Q_m \rangle$, $\langle Q_S \rangle$, and $\langle Q_L \rangle$ obtained in DNS in (x,z) plane.

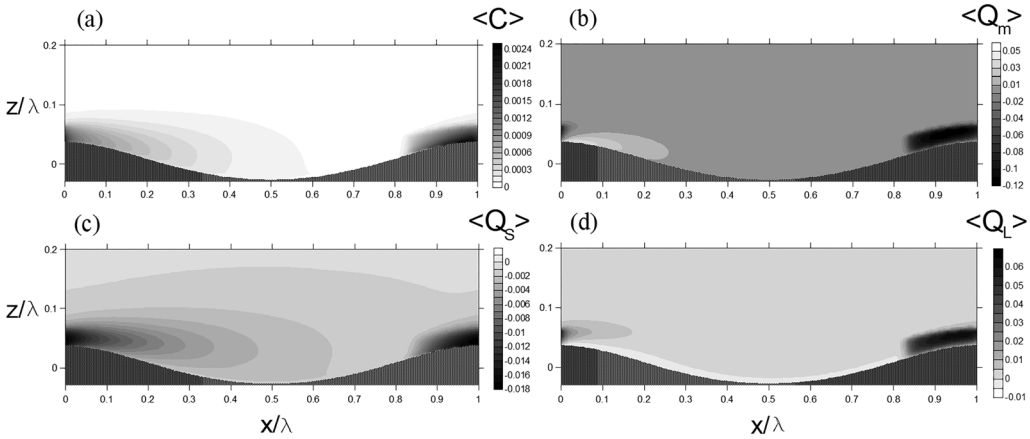

Figure 7. Phase-averaged droplets concentration,⟨*C*⟩ (a); momentum flux, ⟨Q_m⟩, (b); sensible heat flux, ⟨Q_S⟩, (c); and latent heat flux, ⟨Q_L⟩, (d). Droplets mass fraction C_m = 0.038. Here and below in Figure 8 fluxes are from the droplets to the air.

Figure 7 shows that in both cases, droplets concentration as well as momentum and heat fluxes peaks are in the vicinity of the upwind side of the surface wave crests. The momentum flux, ⟨Q_m⟩, is positive at the lee-side of the wave crest and negative at the upwind side of the crest (Figures 6a and 6b). The latter observation is explained by the transfer of momentum from air to drops during their acceleration by the wind immediately after injection, whereas positive ⟨Q_m⟩ is due to the transfer of momentum to the air from large drops during their descent toward the water surface (cf. Figure 6d). Since droplets descend toward the water surface and have *finite* inertia, its horizontal *x*-velocities are larger than the surrounding air velocity, thus the positive sign of ⟨Q_m⟩ (cf. Figures 5b and 5d and 6b and 6d). As Figures 7c–7f illustrate, the sensible heat flux, ⟨Q_S⟩, is negative whereas the latent heat flux is mostly positive, and the peak values of ⟨Q_L⟩ far exceed those of ⟨Q_S⟩.

We further obtained mean profiles of the concentration and fluxes, [*C*](*η*) and [$Q_{m,\ S,\ L}$](*η*), by averaging respective phase-averaged distributions over the streamwise coordinate, ξ, as in equation (32). We also evaluated a distance of the drops from the water surface, $\overline{\eta}_d/\lambda$, and the contributions from individual drops to the momentum, sensible, and latent heat fluxes to the air, $\overline{Q}_m^d$, $\overline{Q}_S^d$, and $\overline{Q}_L^d$. The fluxes, equations (40)–(42), were integrated over total simulation time along Lagrangian droplets trajectories and represented as functions of the initial ratio ($V_s/\kappa u_*$; directly related to the initial droplet diameter d_0) by dividing the initial droplets diameter range (100μm ≤ d_0 ≤ 300μm) into 200 bins (thus, each bin of diameter range $d_0 \le d \le d_0 + \Delta d$, Δd = 1μm) and summing up the contributions due to droplets within each bin and normalizing the sum with the number of droplets in the bin ($N_b(d_0)$) as

$$\overline{Q}_{m,S,L}^d = \frac{1}{N_b(d_0)} \sum_{d_0 \le d \le d_0+\Delta d} \int Q_{m,S,L}^d dt. \tag{48}$$

Thus, $\overline{Q}_m^d$, $\overline{Q}_S^d$, and $\overline{Q}_L^d$ represent the net average momentum and heat fluxes as functions of the initial droplet ratio $V_s/\kappa u_*$ (defined by the initial droplet diameter, d_0).

Figure 8 shows the dependence of the average distance of a drop to the water surface, $\overline{\eta}_d/\lambda$, on $V_s/\kappa u_*$ and mean profile of the drops concentration, [*C*], and distributions and mean profiles of feedback fluxes of momentum and latent and sensible heat. As can be deduced from Figure 8a, the mean height of the drop above the water surface decreases with $V_s/\kappa u_*$, so that drops with $V_s/\kappa u_* > 1$ ($d > 200$ μm) are found mostly in the near-water surface layer, at $\eta/\lambda < 0.1$. These drops provide the most significant contribution to the concentration, [*C*], which becomes negligible at heights $\eta/\lambda > 0.1$ (or, in wall-scale-normalized units, at ηu_* Re > 50), that is, in the logarithmic region of the boundary layer.

Figure 8c shows that the momentum flux obtained by integration over time along Lagrangian trajectories of individual drops, $\overline{Q}_m^d$, is near zero for drops with $V_s/\kappa u_* < 1$, negative for larger drops and enhanced with increasing $V_s/\kappa u_*$. Thus, on average, only sufficiently large drops contribute to the spray-mediated momentum flux and act as a sink of the air momentum. The mean net momentum flux, [Q_m], obtained by

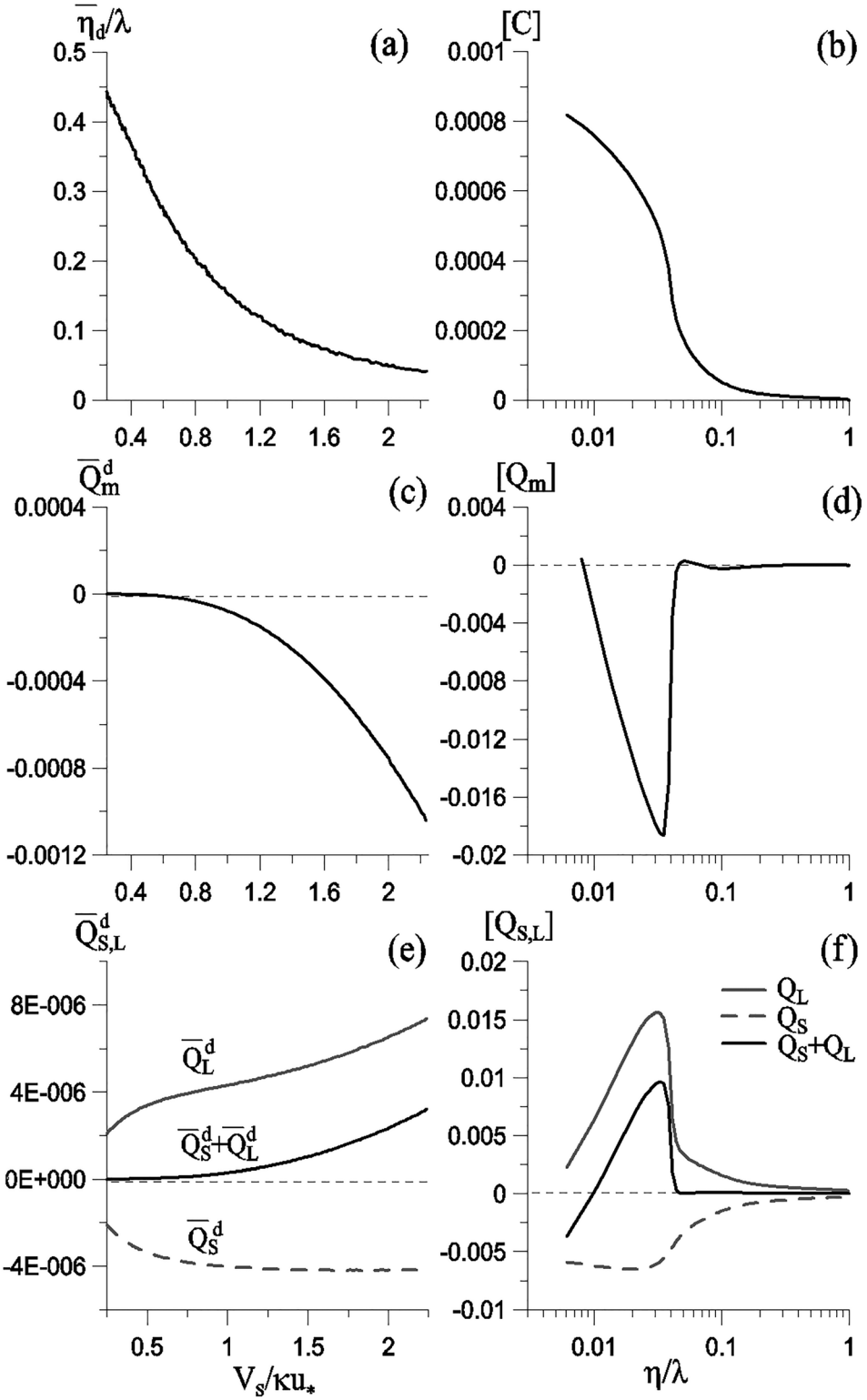

Figure 8. Size (i.e., initial $V_s/\kappa u_*$) distributions (left column) and mean profiles (right column) of drops height over water surface, $\overline{\eta}_d$, (a); drops concentration, $[C]$, (b); momentum flux from drops to air, $\overline{Q}_m^d$ (c), and $[Q_m]$ (d); and sensible and latent and enthalpy fluxes, $\overline{Q}_{L,S}^d$ and $\overline{Q}_L^d + \overline{Q}_S^d$, (e) and $[Q_{L,\,S}]$, $[Q_L + Q_S]$ (f). Fluxes $\overline{Q}_{m,L,S}^d$ are obtained by integration over individual droplets Lagrangian trajectories, whereas fluxes $[Q_{m,\,L,\,S}]$ are obtained by summation over all droplets, phase-averaging and averaging over the wave length.

summation of all drops contributions and phase (i.e., ensemble) averaging and averaging over the wave length is negligible in close vicinity of the water surface, at $\eta/\lambda < 0.01$ (i.e., in the viscous sublayer), decreases with height, becomes negative and peaks at $\eta/\lambda \approx 0.03$, in the buffer region of the boundary layer (Figure 8d). $[Q_m]$ further jumps back to near-zero for $0.04 < \eta/\lambda < 0.05$ and becomes negligible at heights $\eta/\lambda > 0.06$. Thus, as the figure illustrates, the net feedback effect of the drops results in an additional drag on the air flow.

Figures 8f and 8e present the $(V_s/\kappa u_*)$ distribution and mean profiles of sensible and latent heat fluxes, $\overline{Q}^d_{S,L}$ and $\left[Q^d_{S,L}\right]$, and the enthalpy flux, $\overline{Q}^d_S + \overline{Q}^d_L$ and $[Q_S + Q_L]$, respectively. Figure 8f shows that for sufficiently small drops (i.e., for $V_s/\kappa u_* < 1$) $\overline{Q}^d_S$ is negative, whereas $\overline{Q}^d_L$ is positive and their sum is near zero, $\overline{Q}^d_S + \overline{Q}^d_L \approx 0$. Thus, these drops on average are in the wet bulb state and provide a negligible enthalpy flux to the air. With increasing ratio $V_s/\kappa u_*$ (proportional to the drop size), the latent heat flux increases whereas the sensible heat flux saturates for drops with $V_s/\kappa u_* > 1$ (i.e., for $d > 200\mu$m). As a result, the enthalpy flux increases with the drop size for $V_s/\kappa u_* > 1$. Figures 4c and 4e, 5c and 5e, and 6c and 6e show that the time interval where the sensible heat flux from droplet to air, Q_S, is negative is much shorter than the time interval where Q_S is negative (by two orders of magnitude for the droplet with $V_s/\kappa u_* = 1$ in Figure 5 and by about 20 times for the droplet with $V_s/\kappa u_* = 2.25$). The figures also show that the negative Q_S is also larger than the positive Q_S contribution. This behavior of the sensible flux is consistent with the observed behavior of the average flux $\overline{Q}^d_S$ in Figure 8. The observed saturation of $\overline{Q}^d_S$ for drops with $V_s/\kappa u_* > 1$ can be related to their shorter residence time in the air. The behavior of the drop-mediated latent and sensible heat fluxes in Figure 8 is also consistent with the observation by Peng and Richter (2017) that small droplets add as much latent heat flux as they take away from the sensible heat flux, whereas large droplets (with $V_s/\kappa u_* > 1$ and relatively short residence times) do not reach the equilibrium temperature as quickly, and so can contribute to the enthalpy flux.

Figure 8f shows that in close vicinity of the water surface, at $\eta/\lambda < 0.01$, the sensible heat flux, $[Q_S]$, is negative whereas the latent heat flux, $[Q_L]$, is positive and relatively small so that the resulting enthalpy flux is negative. This behavior of $[Q_S]$ and $[Q_L]$ is in accord with the above-discussed dynamics of sufficiently large drops (with ratio $V_s/\kappa u_* > 1$) which fall into the water at temperatures far below the surrounding air temperature (which in this region is close to the water surface temperature, $T_w = 28$°C). Since local humidity near the water surface is close to the boundary value $H(\eta = 0) = 0.98$, the difference, $(H - H^s)$, governing the drop evaporation rate, equation (16), is relatively small. Thus, the negative contribution of the sensible heat flux dominates over the positive $[Q_L]$-contribution, and renders the enthalpy flux, $[Q_S + Q_L]$, to be negative.

As Figure 8f illustrates, $[Q_L]$ increases in the region $0.01 < \eta/\lambda < 0.03$, and its peak value is almost twice as large as compared to the modulus of $[Q_S]$. On the other hand, the sensible heat flux, $[Q_S]$, is negative and practically constant at distances $\eta/\lambda < 0.03$ and further increases (and the modulus of $[Q_S]$ decreases) with η. As a result, the enthalpy flux, $[Q_S + Q_L]$, is positive at $\eta/\lambda > 0.01$, increases with the distance from the water surface, and peaks at $\eta/\lambda \approx 0.03$ and further decreases to zero at larger η. The reduction of the enthalpy flux at sufficiently large distance from the water surface is in agreement with the data for the distributions of $[Q_L]$ and $[Q_S]$ in Figure 8e and the droplets mean distance from the water surface, $\overline{\eta}_d/\lambda$ in Figure 8a. Figures 2, 8a, and 8e show that sufficiently large drops (with ratio $V_s/\kappa u_* > 1$ and diameter $d > 200\mu$m) are found mostly near the water surface, and mainly these drops contribute to the net enthalpy flux. Therefore, the flux peaks in the vicinity of the water surface, at $\eta/\lambda \approx 0.03$. On the other hand, smaller droplets are found at larger distance from the water surface and in the wet bulb state and do not contribute to the enthalpy flux which therefore is reduced at $\eta/\lambda > 0.04$.

3.3. Modification of the Airflow

In order to elucidate the effects of droplets feedback fluxes on the air flow, we performed DNS of the droplet-free flow (i.e., for drops initial mass fraction $C_m = 0$), with the same bulk parameters, and compared the results with the above-discussed case of $C_m = 0.038$.

Figure 9 compares mean profiles of turbulent momentum, heat, and humidity fluxes obtained in DNS with $C_m = 0$ and $C_m = 0.038$. The figure shows that under the influence of drops, (a) turbulent momentum flux, $[\tau_m]$, and (b) velocity fluctuations are reduced in close vicinity of the water surface, at $\eta/\lambda < 0.05$ (or $\eta^+ < 15$, i.e., in the viscous sublayer and buffer region), whereas (d) temperature fluctuation, $[T']$, is increased in this

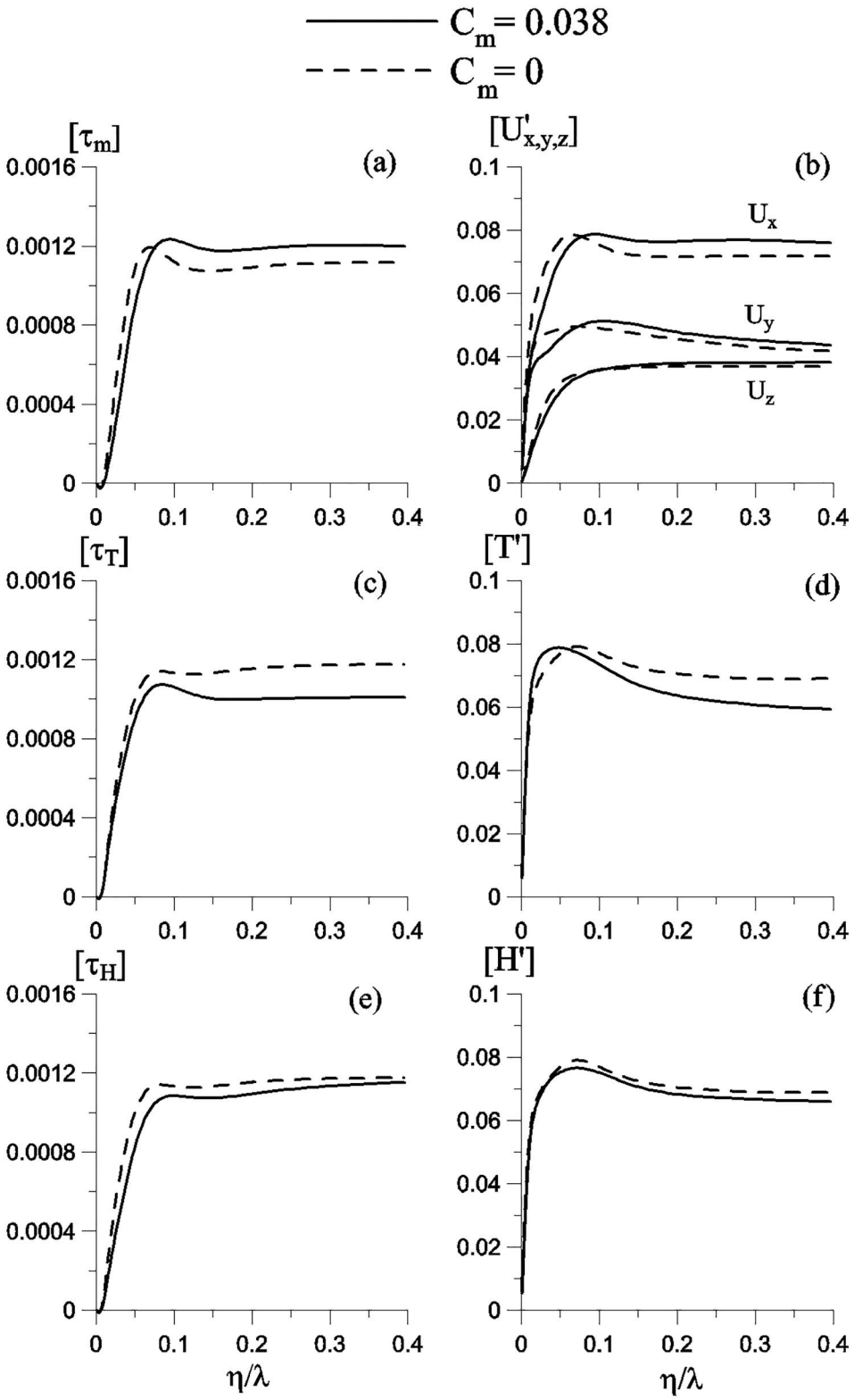

Figure 9. Vertical profiles of the fluxes of air turbulent momentum (a), heat (c), and moisture (e) and RMS fluctuations of *x*, *y*, *z* components of air velocity (b), temperature (d), and humidity (f) in direct numerical simulation with $C_m = 0$ (droplet-free flow) and $C_m = 0.038$.

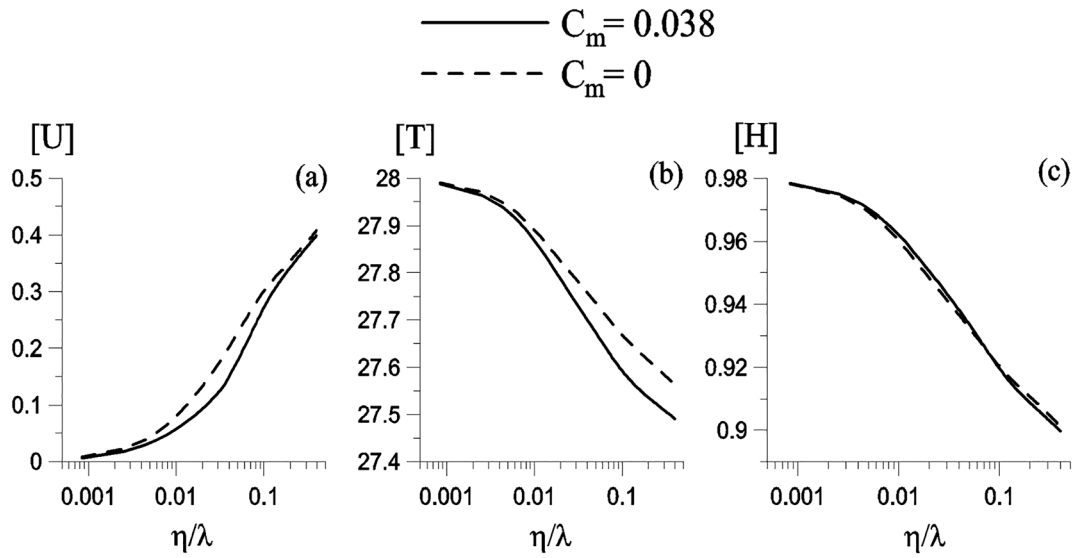

Figure 10. Vertical profiles of the air mean velocity (a), temperature (b), and humidity (c) in direct numerical simulation with $C_m = 0$ (unladen flow) and $C_m = 0.038$.

region as compared to the droplet-free flow. On the other hand, $[\tau_m]$, $\left[U_x^{'}\right]$, and $\left[U_y^{'}\right]$ are increased, and $[T^{'}]$ is reduced at larger heights, at $\eta/\lambda < 0.1$ (in the logarithmic layer). The figure shows also that heat and humidity fluxes, $[\tau_T]$ and $[\tau_H]$, as well as humidity fluctuations, $[H^{'}]$, are reduced throughout the flow domain as compared to the unladen-flow case.

Figure 10 presents mean profiles of air velocity, temperature, and relative humidity obtained in DNS of droplet-free ($C_m = 0$) and droplet-laden ($C_m = 0.038$) flows. As the figure illustrates, droplets reduce mean air velocity and temperature, $[U]$ and $[T]$, and increase relative humidity, $[H]$. Data in Figure 10 are in accord with the behavior of drops-mediated fluxes in Figure 8. The data are also in qualitative agreement with the field observations of air-temperature reduction of the air in the vicinity of the water surface under strong winds (cf. e.g., Fairall et al., 1994).

4. Discussion and Conclusions

In the present paper, we have performed DNS of a turbulent airflow laden with evaporating, spherical droplets over a waved water surface. Three-dimensional, turbulent Couette airflow is considered in DNS as a model of a constant-stress layer of the atmospheric boundary layer. Two-dimensional, stationary wave at the water surface is prescribed and assumed to be unaffected by the airflow and/or drops. Evaporating, spherical droplets which are injected into the air flow in the vicinity of wave crests with initial velocities and temperatures equal to those of water, and thus mimic spume sea-spray drops torn off the wave crests by the wind. The air-water bulk temperature and relative humidity differences considered in DNS are analogous to these parameters formulated by Andreas and Emanuel (2001). Evolution equations of the airflow velocity, temperature, and humidity are solved in a Eulerian framework simultaneously with the equations of individual droplets coordinates and velocities, temperatures, and masses tracked in a Lagrangian framework. The impact of droplets on the airflow is modeled via a point-force approximation, and both momentum and latent and sensible heat exchange between droplets and air are taken into account. Momentum (Q_m) and sensible (Q_S) and latent (Q_L) heat fluxes from the droplets to the air are evaluated both as phase-averaged Eulerian fields and as fluxes averaged over time along Lagrangian trajectories of individual droplets.

The Lagrangian statistics obtained in DNS shows that droplets on average extract momentum from the surrounding air during their motion (i.e., $Q_m < 0$), and this sink of momentum is more pronounced for larger droplets. The latent heat flux, Q_L, integrated along the trajectories of droplets of different sizes, is positive and increases with ratio of the gravitational settling velocity versus the product of the friction velocity and the

Karman constant ($V_s/\kappa u_*$; also proportional to the droplet diameter, d). The sensible heat flux, Q_S, is negative, reaches maximum for droplets with ratio $V_s/\kappa u_* \approx 1$ (or equivalently, for drops diameter $d \approx 200\mu$m), and saturates for droplets with larger $V_s/\kappa u_*$. The resulting enthalpy flux, measured by the sum ($Q_S + Q_L$), vanishes for sufficiently small droplets, whose ratio $V_s/\kappa u_* \ll 1$ and diameter $d \ll 200$ μm, since these droplets are in the wet bulb state for the most time during their motion in the air. However, the enthalpy flux but becomes positive and increases with diameter for droplets whose ratio $V_s/\kappa u_* > 1$ and $d > 200\mu$m.

The Eulerian statistics shows that the mean droplets concentration, C, as well as momentum and enthalpy fluxes ($Q_m < 0$ and $Q_S + Q_L > 0$) are most pronounced in the viscous sublayer and buffer region of the boundary layer, populated by large drops whose ratio $V_s/\kappa u_* > 1$. Both C and Q_m and $Q_S + Q_L$ decrease to zero in the logarithmic region which is populated mainly by small droplets with ratio $V_s/\kappa u_* << 1$, who thus provide a negligible net contribution to the total drops volume fraction and both momentum and enthalpy feedback fluxes. DNS results also show that droplets reduce mean air velocity and temperature and increase relative humidity as compared to the droplet-free flow.

It is important to point out that the observed reduction of the airflow momentum by the droplets in DNS is related to the particular scenario of droplet injection considered in the present study. The results of our previous study (Druzhinin et al., 2017) show that droplets dynamics, as well as the net feedback momentum flux, are extremely sensitive to droplets velocities at injection: droplets injected with the surrounding air velocity accelerate the carrier flow, whereas droplets injected with the surface wave velocity decelerate the flow. In the present study, we use experimentally observed facts indicating that spume droplets are primarily injected into the airflow in the vicinity of the wave crests. Unfortunately, the droplets velocities distribution at injection is still unknown. Thus, in the present study, we follow Andreas and Emanuel (2001) and Andreas (2004) and inject droplets with initial velocities equal to the velocities of fluid particles in the surface wave, and the results are consistent with those obtained by Druzhinin et al. (2017). Recent study by Troitskaya, Kandaurov, et al. (2018) suggests that the dominant mechanism of spume droplets generation is that of a bag-breakup fragmentation. Troitskaya et al. (2017) and Troitskaya, Druzhinin, et al. (2018) developed a statistical description of the bag-breakup phenomena, but PDF of the drops velocities at injection still remains unknown and requires further research. Thus, we need to clarify the details of the droplets injection mechanism and further incorporate these details into DNS procedure. In the present study we also do not take into account an additional roughness of the water surface introduced by the presence of bags. Incorporating in DNS an updated (although, yet unknown) droplets injection mechanism as well as taking into account an additional roughness of the water surface caused by the presence of bags as obstacles is a challenging task for future research and out of the scope of the present study.

To our knowledge, so far there have been no published DNS studies of a turbulent, droplet-laden boundary layer flow over a waved water surface where momentum and latent and sensible heat exchanges between the air and drops are *simultaneously* taken into account. Therefore, the present study should be considered as a first step in employing DNS for modeling spray-mediated momentum, heat, and mass transfer in the marine atmospheric boundary layer. It should be emphasized however that the Reynolds number considered in our DNS is far below the one observed in natural conditions. Thus, the present study can be regarded only as a scaled mathematical model providing qualitative understanding of the drop-mediated momentum and heat exchange processes occurring in the marine atmospheric boundary layer at strong wind forcing in natural conditions.

Acknowledgments
We are grateful to the anonymous referees for all comments and suggestions. This work is supported by RFBR (16-55-52022, 16-05-00839, 17-05-00703, 18-05-00265, 18-55-50005) and by the Russian Science Foundation (14-17-00667, 15-17-20009). S.Z. additionally acknowledges support from the Academy of Finland project ClimEco No. 314 798/799. Description of numerical and postprocessing algorithms and necessary data files discussed in the present paper are available at http://www.iapras.ru.

References

Andreas E. L. (1989). Thermal and size evolution of sea spray droplets. CRREL Rep. 89-11, 47 pp.

Andreas, E. L. (1992). Sea spray and the turbulent air–sea heat fluxes. *Journal of Geophysical Research*, *97*, 11,429–11,441. https://doi.org/10.1029/92JC00876

Andreas, E. L. (1995). The temperature of evaporating sea spray droplets. *Journal of the Atmospheric Sciences*, *52*, 852–862. https://doi.org/10.1175/1520-0469(1995)052<0852:TTOESS>2.0.CO;2

Andreas, E. L. (2004). Spray stress revisited. *Journal Physical Oceanography*, *34*, 1429–1440. https://doi.org/10.1175/1520-0485(2004)034<1429:SSR>2.0.CO;2

Andreas, E. L. (2013). An algorithm for fast microphysical calculations that predict the evolution of saline droplets. NorthWest Research Associates. Retrieved from https://people.nwra.com/resumes/andreas/software.php

Andreas, E. L., & Emanuel, K. A. (2001). Effects of sea spray on tropical cyclone intensity. *Journal of the Atmospheric Sciences*, *58*, 3741–3751. https://doi.org/10.1175/1520-0469(2001)058<3741:EOSSOT>2.0.CO;2

Andreas, E. L., Jones, K. F., & Fairall, C. W. (2010). Production velocity of sea spray droplets. *Journal of Geophysical Research*, *115*, C12065. https://doi.org/10.1029/2010JC006458

Balachandar, S., & Maxey, M. R. (1989). Methods for evaluating fluid velocities in spectral simulations of turbulence. *Journal of Computational Physics*, *83*, 96–125. https://doi.org/10.1016/0021-9991(89)90224-6

Bao, J.-W., Fairall, C. W., Michelson, S. A., & Bianco, L. (2011). Parameterizations of sea-spray impact on the air–sea momentum and heat fluxes. *Monthly Weather Review*, *139*(12), 3781–3797. https://doi.org/10.1175/MWR-D-11-00007.1

Borisenkov, E. E. (1974). Some mechanisms of atmosphere-ocean interaction under stormy weather conditions. *Problems Arctic Antarctic*, *43-44*, 73–83.

Bortkovskii, R. S. (1973). On the mechanism of interaction between the ocean and the atmosphere during the storm. *Fluid Mechanics - Soviet Research*, *2*, 87–94.

Bortkovskii, R. S. (1987). *Air-sea exchange of heat and moisture during storms*. Ed. by E.C. Monahan. Dodrecht: D. Reidel. 206 pp. https://doi.org/10.1007/978-94-017-0687-2

Buck, A. L. (1981). New equation for computing vapor pressure and enhancement factor. *Journal of Applied Meteorology*, *20*, 1527–1532. https://doi.org/10.1175/1520-0450(1981)020<1527:NEFCVP>2.0.CO;2

Clift, R., Grace, J. R., & Weber, M. E. (1978). *Bubbles, drops, and particles* (p. 369). New York, San Francisco, London: Academic Press.

Druzhinin, O. A. (2001). The influence of particle inertia on the two-way coupling and modification of isotropic turbulence by microparticles. *Physics of Fluids*, *13*, 3738–3755. https://doi.org/10.1063/1.1415735

Druzhinin, O. A., Troitskaya, Y. I., & Zilitinkevich, S. S. (2016). Stably stratified airflow over a waved water surface. Part 1: Stationary turbulence regime. *Quarterly Journal of the Royal Meteorological Society*, *142*, 759–772. https://doi.org/10.1002/qj.2677

Druzhinin, O. A., Troitskaya, Y. I., & Zilitinkevich, S. S. (2017). The study of droplet-laden turbulent air flow over waved water surface by direct numerical simulation. *Journal of Geophysical Research: Oceans*, *122*, 1789–1807. https://doi.org/10.1002/2016JC012134

Druzhinin, O. A., Troitskaya, Y. I., & Zilitinkevish, S. S. (2012). Direct numerical simulation of a turbulent wind over a wavy water surface. *Journal of Geophysical Research*, *117*, C00J05. https://doi.org/10.1029/2011JC007789

Edson, J. B., & Fairall, C. W. (1994). Spray droplet modeling: 1. Lagrangian model simulation of the turbulent transport of evaporating droplets. *Journal of Geophysical Research*, *99*, 25,295–25,311. https://doi.org/10.1029/94JC01883

Fairall, C. W., Banner, M. L., Peirson, W. L., Asher, W., & Morrison, R. P. (2009). Investigation of the physical scaling of sea spray spume droplet production. *Journal of Geophysical Research*, *114*, C10001. https://doi.org/10.1029/2008JC004918

Fairall, C. W., Kepert, J. D., & Holland, G. J. (1994). The effect of sea-spray on surface energy transports over the ocean. *The Global Atmosphere and Ocean System*, *2*, 121–142.

Gelfand, B. E. (1996). Droplet breakup phenomena in flows with velocity lag. *Progress in Energy and Combustion Science*, *22*, 201–265. https://doi.org/10.1016/S0360-1285(96)00005-6

Gent, P. R., & Taylor, P. A. (1976). A numerical model of the air flow above water waves. *Journal of Fluid Mechanics*, *77*, 105–128. https://doi.org/10.1017/S0022112076001158

Helgans, B., & Richter, D. H. (2016). Turbulent latent and sensible heat flux in the presence of evaporative droplets. *International Journal of Multiphase Flow*, *78*, 1–11. https://doi.org/10.1016/j.ijmultiphaseflow.2015.09.010

Kudryavtsev, V. N. (2006). On the effects of sea on the atmospheric boundary layer. *Journal of Geophysical Research*, *111*, C07020. https://doi.org/10.1029/2005JC002970

Kudryavtsev, V. N., & Makin, V. K. (2011). Impact of ocean spray on the dynamics of the marine atmospheric boundary layer. *Boundary-Layer Meteorology*, *140*, 383–410. https://doi.org/10.1007/s10546-011-9624-2

Ling, S. C., & Kao, T. W. (1976). Parameterization of the moisture and heat transfer process over the ocean under whitecap sea states. *Journal of Physical Oceanography*, *6*, 306–315. https://doi.org/10.1175/1520-0485(1976)006<0306:POTMAH>2.0.CO;2

Maxey, M. R., & Riley, J. J. (1983). Equation of motion for a small rigid sphere in a non-uniform flow. *Physics of Fluids*, *26*, 49–60.

Monin, A. S., & Yaglom, A. M. (1971). *Statistical fluid mechanics: Mechanics of turbulence* (Vol. 1, p. 769). Cambridge, Massachusetts, and London, England: MIT Press.

Mueller, J. A., & Veron, F. (2014). Impact of sea spray on air–sea fluxes. Part I: Results from stochastic simulations of sea spray drops over the ocean. *Journal of Physical Oceanography*, *44*, 2817–2834. https://doi.org/10.1175/JPO-D-13-0245.1

Peng, T., & Richter, D. (2017). Influence of evaporating droplets in the turbulent marine atmospheric boundary layer. *Boundary-Layer Meteorology*, *165*, 1–22.

Pruppacher, H. R., & Klett, J. D. (1978). *Microphysics of clouds and precipitation* (p. 714). Dordrecht: D. Riedel. https://doi.org/10.1007/978-94-009-9905-3

Richter, D. H., & Sullivan, P. P. (2013). Sea surface drag and the role of spray. *Geophysical Research Letters*, *40*, 656–660. https://doi.org/10.1002/grl.50163

Richter, D. H., & Sullivan, P. P. (2014). The sea spray contribution to sensible heat flux. *Journal of the Atmospheric Sciences*, *71*(2), 640–654. https://doi.org/10.1175/JAS-D-13-0204.1

Sullivan, P. P., McWilliams, J. C., & Moeng, C.-H. (2000). Simulation of turbulent flow over idealized water waves. *Journal of Fluid Mechanics*, *404*, 47–85. https://doi.org/10.1017/S0022112099006965

Troitskaya, Y., Kandaurov, A., Ermakova, O., Kozlov, D., Sergeev, D., & Zilitinkevich, S. (2017). Bag-breakup fragmentation as the dominant mechanism of sea-spray production in high winds. *Scientific Reports*, *7*, 1614. https://doi.org/10.1038/s41598-017-01673-9

Troitskaya, Y., Druzhinin, O., Kozlov, D., & Zilitinkevich, S. (2018). The "bag breakup" spume droplet generation mechanism at high winds. Part II. Contribution to momentum and enthalpy transfer. *Journal of Physical Oceanography*, *114*(C10), 2189–2207. https://doi.org/10.1029/2008JC004918

Troitskaya, Y., Kandaurov, A., Ermakova, O., Kozlov, D., Sergeev, D., & Zilitinkevich, S. (2018). The "bag breakup" spume droplet generation mechanism at high winds. Part I: Spray generation function. *Journal of Physical Oceanography*, *48*, 2167–2188. https://doi.org/10.1175/JPO-D-17-0104.1

Troitskaya, Y. I., Ezhova, E. V., Soustova, I. A., & Zilitinkevich, S. S. (2016). On the effect of sea spray on the aerodynamic surface drag under severe winds. *Ocean Dynamics*, *66*, 659–669. https://doi.org/10.1007/s10236-016-0948-9

Veron, F., Hopkins, C., Harrison, E. L., & Mueller, J. A. (2012). Sea spray spume droplet production in high wind speeds. *Geophysical Research Letters*, *39*, L16602. https://doi.org/10.1029/2012GL052603

Wu, J. (1974). Evaporation due to spray. *Journal of Geophysical Research*, *79*, 4107–4109. https://doi.org/10.1029/JC079i027p04107

Yang, D., & Shen, L. (2010). Direct-simulation-based study of turbulent flow over various waving boundaries. *Journal of Fluid Mechanics*, *650*, 131–180. https://doi.org/10.1017/S0022112009993557